Short Note

A Magnitude Attenuation Function Derived for the 2014 Pisagua (Chile) Sequence Using Strong-Motion Data

by D. Bindi, B. Schurr, R. Puglia, E. Russo, A. Strollo, F. Cotton, and S. Parolai

Abstract   In this note, we derive an attenuation function for computing magnitude values equivalent to M_w using strong-motion data. We analyze 106 earthquakes of the 1 April 2014 M_w 8.1 Pisagua sequence, which occurred along the 1877 seismic gap in northern Chile. We considered both foreshocks and aftershocks with moment magnitude available from moment tensor inversion in the GEOFON bulletin and recorded by the Integrated Plate boundary Observatory Chile strong-motion network. The maximum peak displacement measured over the double integrated traces is used to construct the magnitude scale, following a nonparametric approach. A bootstrap analysis is performed to assess the uncertainty of the model parameters, and cross-validation tests are performed to proof the suitability of the derived model in predicting the M_w in the analyzed area, with an uncertainty of 0.2 magnitude units. The derived scale is applied to an early aftershock, which occurred about 155 s after the mainshock, initially missed in bulletins published by rapid global earthquake monitoring agencies (e.g., National Earthquake Information Center and GEOFON), because its phase arrivals at regional/teleseismic distances mix with those of the mainshock and its later arrivals. The estimated magnitude equivalent to M_w is 6.6 ± 0.3, which rank this event as the second largest aftershock of the sequence, after the M_w 7.6 earthquake that occurred on 3 April 2014.

Data

We analyze strong-motion data of the seismic sequence associated with the 1 April 2014 M_w 8.1 Pisagua earthquake (northern Chile). Tectonics in this area is controlled by the subduction of the Nazca plate beneath the South American plate (e.g., Schurr *et al.*, 2014). The zone from about 18° to 23° S has been identified as a seismic gap because no large earthquakes have occurred there since 1877 (Kelleher, 1972), and the current rate of the Nazca plate underthrusting is about 65 mm/yr (DeMets *et al.*, 2010).

The data set considered here is composed of earthquakes that occurred since January 2014, including a protracted foreshock sequence that culminated in an M_w 6.7 event in March 2014, two weeks before the Pisagua mainshock and aftershocks, which occurred until the end of April 2014. Only earthquakes with location and moment magnitude from the GEOFON bulletin (see Data and Resources) have been selected. In total, for each component of motion, 1049 waveforms from 106 earthquakes in the moment magnitude range of 4.5–8.1 and recorded by 15 strong-motion stations of the Integrated Plate boundary Observatory Chile (IPOC) network (see Data and Resources) compose the data set. Figure 1 shows the source-to-station path coverage for our data set, and Table 1 lists the main character-istics of the considered stations. The magnitude versus hypocentral distance and magnitude versus source-to-station azimuth scatter plots are shown as well. The hypocentral distances cover the range 50–300 km, with magnitude smaller than five detected up to a maximum distance of 200 km in the considered data set. As expected from the tectonic setting, the source-to-station azimuths span the interval mainly from 0° to 180° with respect to north. About 85% of data corresponds to magnitudes smaller than six, with the three largest magnitudes corresponding to the 16 March M_w 6.7 foreshock, the 1 April M_w 8.1 mainshock, and the 3 April M_w 7.6 aftershock.

The strong-motion data were processed according to the methodology used by Paolucci *et al.* (2011) and were integrated to both velocity and displacement. The corner frequencies of the applied high-pass acausal Butterworth filter were set to 0.2 Hz for earthquakes with $M_w \leq 5.5$ and to 0.1 Hz for $5.5 < M_w \leq 6.0$. These frequencies were selected after the visual inspection of several Fourier spectra of recordings relevant to different magnitude and distance ranges. Conversely, for earthquakes with $M_w > 6.0$, an *ad hoc* selection of the corner frequency was performed for each specific recording. For example, the corner frequencies for the
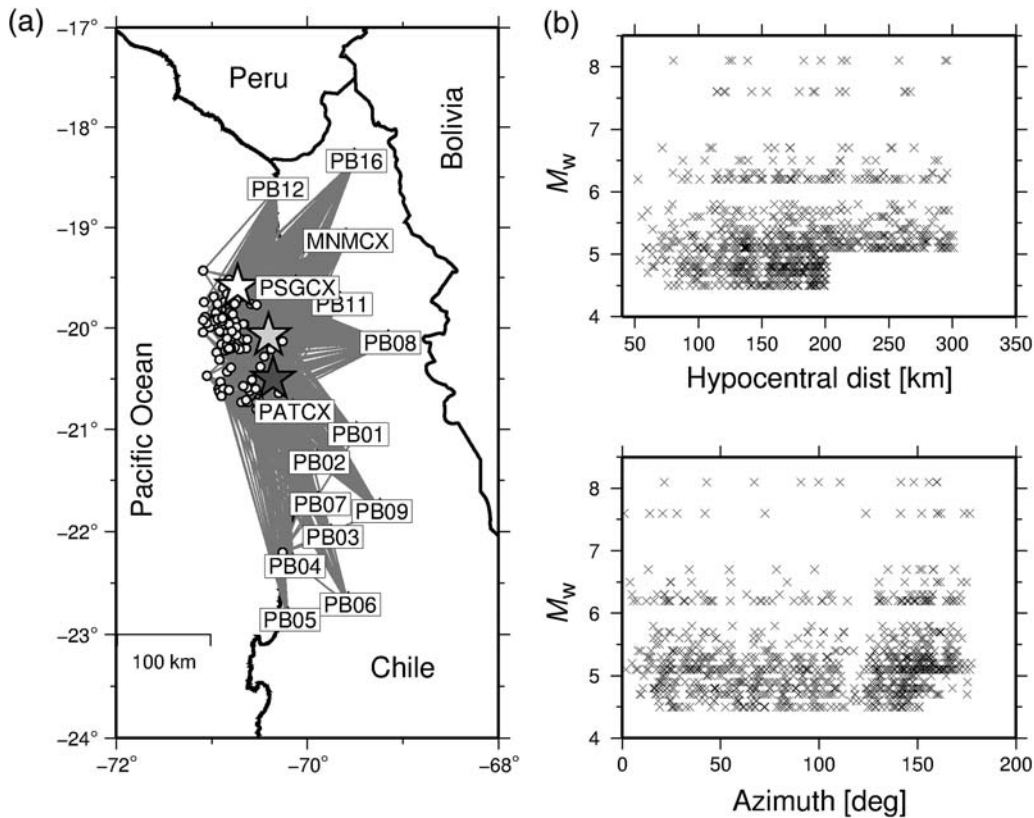
Figure 1. (a) The map showing the earthquake locations (empty circles), the station locations (station names as listed in Table 1), and the source-to-station path coverage (gray lines). The star symbols indicate the location of the M_w 8.1 mainshock (white), the M_w 7.6 aftershock (dark gray), and the aftershock discussed in the Application and Conclusions section (light gray). (b) Moment magnitude versus hypocentral distance (top) and moment magnitude versus source-to-station azimuth (bottom) scatter plots.

M_w 8.1 mainshock vary in the 0.01–0.03 Hz range. Figure 2 shows the acceleration spectra for three recordings and the selected corner frequencies. The displacement time histories obtained after double integration of the filtered accelerations are shown as well.

Attenuation Function

The evaluation of the magnitude at local distances requires the calibration of a model describing the seismic attenuation in the study area. This is necessary because importing

Table 1
Selection of Integrated Plate Boundary Observatory Chile Stations Used in This Study.

ID	Name	Latitude (°)	Longitude (°)	Elevation (m)	Correction	±95% CI
1	MNMCX	−19.1311	−69.5955	2304	0.16	0.06
2	PATCX	−20.8207	−70.1529	832	0.10	0.07
3	PB01	−21.0432	−69.4874	900	−0.07	0.05
4	PB02	−21.3197	−69.896	1015	0.12	0.05
5	PB03	−22.0485	−69.7531	1460	−0.15	0.07
6	PB04	−22.3337	−70.1492	1520	0.09	0.07
7	PB05	−22.8528	−70.2024	1150	−0.12	0.11
8	PB06	−22.7058	−69.5719	1440	−0.04	0.10
9	PB07	−21.7267	−69.8862	1570	−0.03	0.05
10	PB08	−20.1411	−69.1534	3060	−0.18	0.06
11	PB09	−21.7964	−69.2419	1530	0.14	0.06
12	PB11	−19.761	−69.6558	1400	0.08	0.06
13	PB12	−18.6141	−70.3281	908	0.01	0.05
14	PB16	−18.3351	−69.5077	4480	0.07	0.07
15	PSGCX	−19.5972	−70.1231	966	−0.18	0.07

The mean magnitude correction and its 95% confidence interval (CI) estimated from bootstrap analysis are also shown (see text for details).
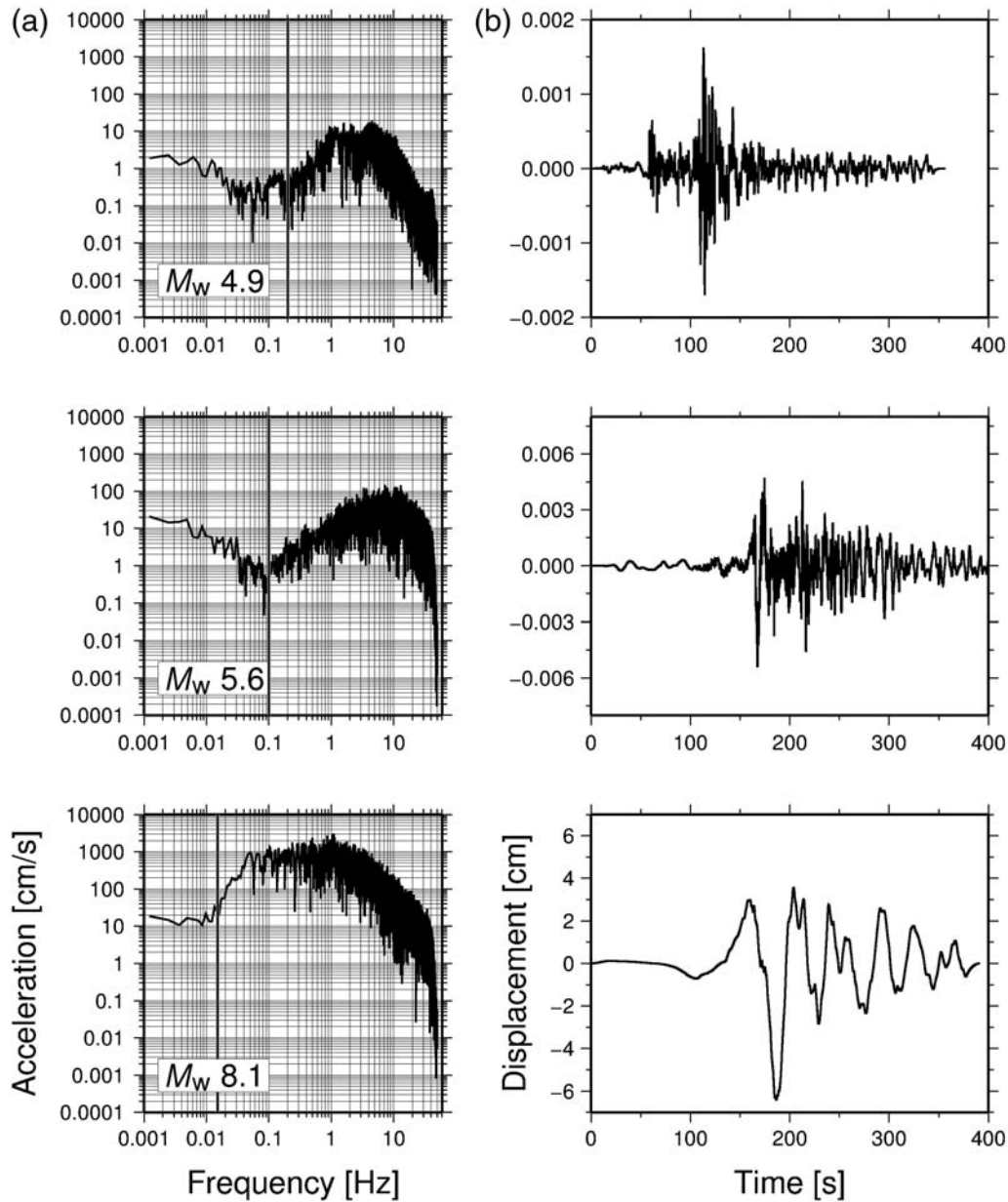
Figure 2.   (a) The example of Fourier amplitude spectra for three recordings of earthquakes with different magnitude as indicated inside each panel. The vertical lines indicate the high-pass corner frequencies used to filter the data. (b) Displacement–time histories obtained after double integration of the filtered acceleration recordings shown in (a).

models from other tectonic setting could introduce a bias in the estimates (e.g., an overestimation when the crustal model calibrated for California is applied). We follow a nonparametric approach (e.g., Savage and Anderson, 1995; Spallarossa *et al.*, 2002; Bindi *et al.*, 2007), in which the attenuation is provided in a tabular form without fixing *a priori* the functional dependence on distance. Each value corresponds to the attenuation at one node of the discretized distance range. The moment magnitudes M_w of the earthquakes considered for the calibration are used to derive an attenuation model that links the logarithm (in base 10) of the amplitude measurements $\log A$ to this magnitude scale. We tested different

choices for $\log A$, namely the maximum amplitude computed over the acceleration trace (peak ground acceleration), velocity trace (peak ground velocity), displacement trace (peak ground displacement [PGD]), and over the synthetic Wood–Anderson seismograms, as generally done when calibrating a local-magnitude scale. Among the different tested choices, we selected the maximum displacement amplitude, because the observation minus prediction residual distribution for PGD does not show significant dependences on both magnitude and distance, as we show in the following. The considered model can be described as
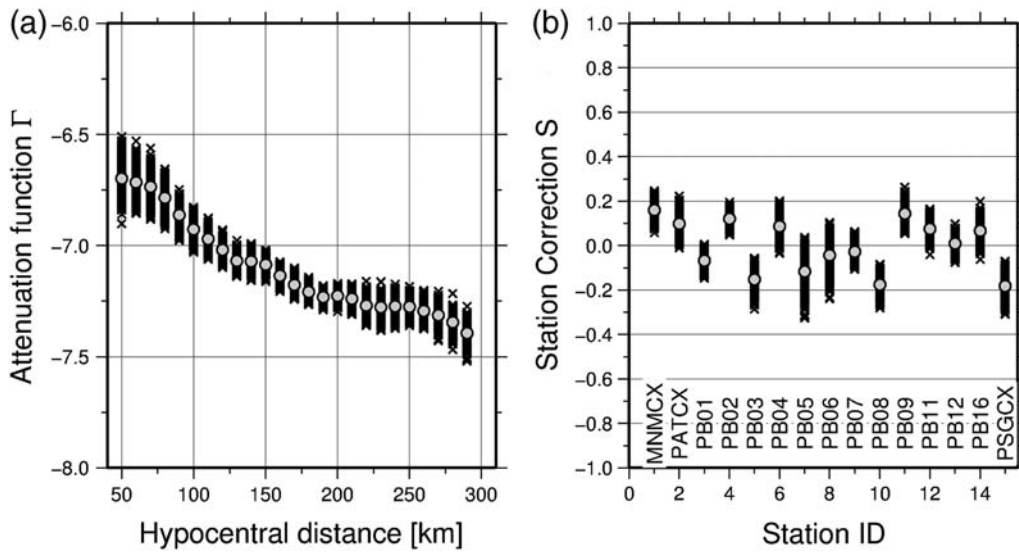
Figure 3. Results of the bootstrap analysis. (a) The attenuation function Γ and (b) the station corrections. Each cross indicates a single bootstrap solution, and the gray circles indicate the mean of their distribution. The station names are also listed in Table 1.

$$\log A_i^j - M_w^j = \Gamma(R_i^j) + S_i, \qquad (1)$$

in which A_i^j is the displacement amplitude in centimeters of an earthquake j recorded at station i; M_w^j is the magnitude of earthquake j; R_i^j is the hypocentral distance in kilometers between station i and earthquake j; and Γ is the discrete version of the attenuation function, and S_i are the station corrections. In this study, the distance range 50–300 km is discretized into bins 10 km wide, and the maximum displacement between the two horizontal components is considered. The attenuation function Γ is evaluated at the nodes R_k of the discretized distance range, and a linear interpolation scheme is applied between adjacent nodes, that is, the attenuation at distance R such that $R_k \leq R < R_{k+1}$ is given by

$$\Gamma(R) = a_k \Gamma(R_k) + a_{k+1} \Gamma(R_{k+1}), \qquad (2)$$

in which the coefficients of the linear interpolation are given by $a_k = (R_{k+1} - R)/(R_{k+1} - R_k)$ and $a_{k+1} = 1 - a_k$.

In the regression scheme, the station corrections S_j are constrained to sum to zero and the attenuation function Γ is constrained to vary smoothly with distance, by requiring a small second derivative, as described in Castro *et al.* (1990). The results presented in this study are obtained by constraining to zero, 10 times the second derivative. A bootstrap sampling technique is applied to estimate the uncertainties (Efron, 1979) by analyzing 1000 different replications of the original data set. Bootstrap methods work by repeated inversions of resampled versions of the original data set. From the original data set, a new one is created by randomly choosing rows from the linear system, in which each row (corresponding to a specific recording) can either be selected several times or never (i.e., random sampling with replications). Figure 3 shows the distribution of the bootstrap solutions (crosses) and the average model (gray circles), listed also in Table 2 along with the 95% confidence intervals of the attenuation values. The attenuation over the analyzed distance range is rather weak (about one order of magnitude of amplitude reduction), with a flattening between 200 and 250 km. The spread of the solution at different distances is generally around 0.2 magnitude units, with an increase to 0.5 at short distances. The station corrections are generally within the range ±0.2, as expected, because most of the installation sites are on rock. The derived attenuation model is

Table 2
Nonparametric Magnitude Attenuation Function Γ(R) and 95% Confidence Interval Obtained from Bootstrap Analysis

R (km)	50	60	70	80	90	100	110	120	130	140	150	160	170
$\Gamma(R)$	−6.70	−6.72	−6.74	−6.79	−6.86	−6.93	−6.97	−7.02	−7.07	−7.07	−7.09	−7.14	−7.18
±95%CI	0.06	0.05	0.04	0.04	0.04	0.03	0.03	0.03	0.03	0.03	0.02	0.02	0.02

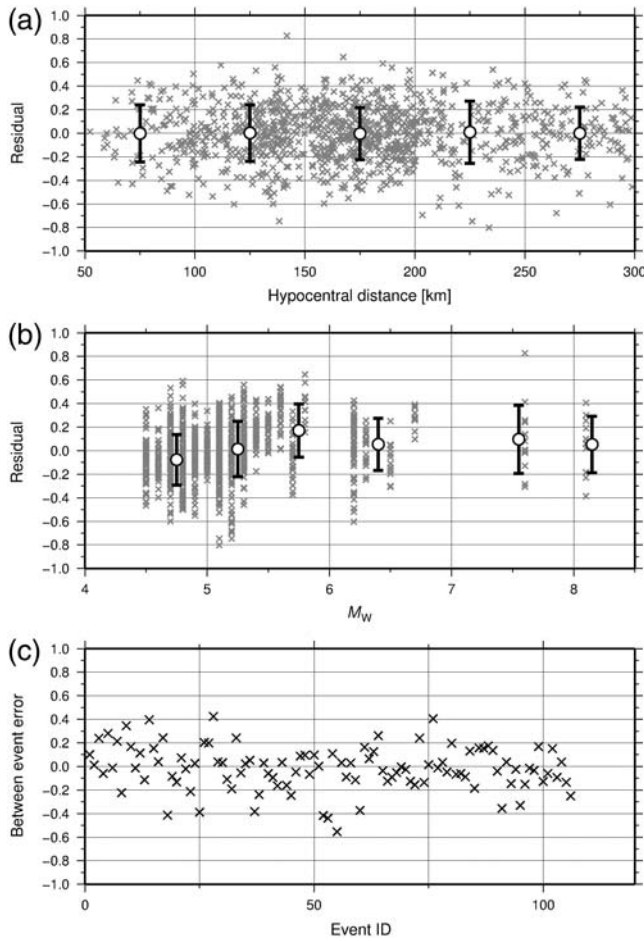| R (km)	180	190	200	210	220	230	240	250	260	270	280	290	300
$\Gamma(R)$	−7.21	−7.23	−7.23	−7.24	−7.27	−7.28	−7.27	−7.27	−7.29	−7.31	−7.34	−7.39	−7.45
±95%CI	0.04	0.04	0.04	0.05	0.06	0.06	0.06	0.05	0.06	0.06	0.06	0.07	0.10

Figure 4. Residual distribution against (a) distance and (b) magnitude, computed as observation–prediction. The average residual ±1 standard deviation computed over either (a) distance or (b) magnitude ranges is also shown (for distance, the intervals are every 50 km and for magnitude, the intervals are 4.5–5, 5–5.5, 5.5–6, and 6–7). (c) The interevent distribution of error is shown for the considered 106 earthquakes.

used to compute the residuals between observations and predictions as shown in Figure 4. The residuals plotted against the explanatory variables (magnitude and distance) do not show significant bias, confirming that the model capture well the main source scaling and attenuation trend. The standard deviation of the error distribution is about 0.2. The residual distribution is decomposed in inter- and intraevent distribution of error (e.g., Al Atik *et al.*, 2010). The interevent errors are generally smaller than 0.3, with a few cases exceeding 0.4. Finally, Figure 5 exemplifies the residual distributions in polar coordinates, considering the hypocentral distance and the back-azimuth values for three selected stations (Fig. 1). Positive (circle) and negative (cross) residuals overlap, without pointing out any azimuth dependence in the residual distribution.

Validation

To perform a cross-validation analysis, the data set is split into two parts, one for calibrating the model and the
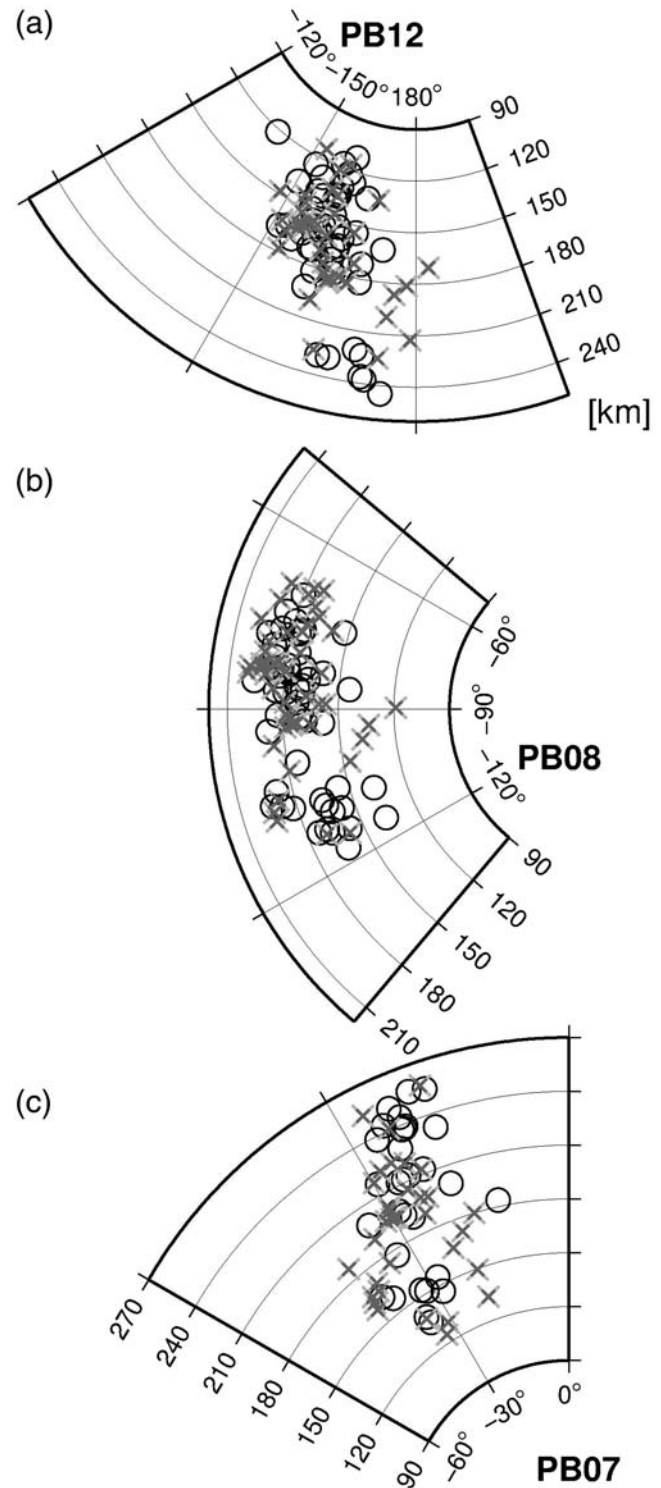

Figure 5. Residuals computed for three stations (PB12, PB08, and PB07, see Fig. 1), considering the hypocentral distance back-azimuth polar coordinates. Positive residuals are shown as circles, whereas crosses indicate negative residuals.

other for its validation using independent information (i.e., waveforms not included in the calibration process). To create the two data sets, a random sampling of the waveforms is performed based on the magnitude values. For calibration,
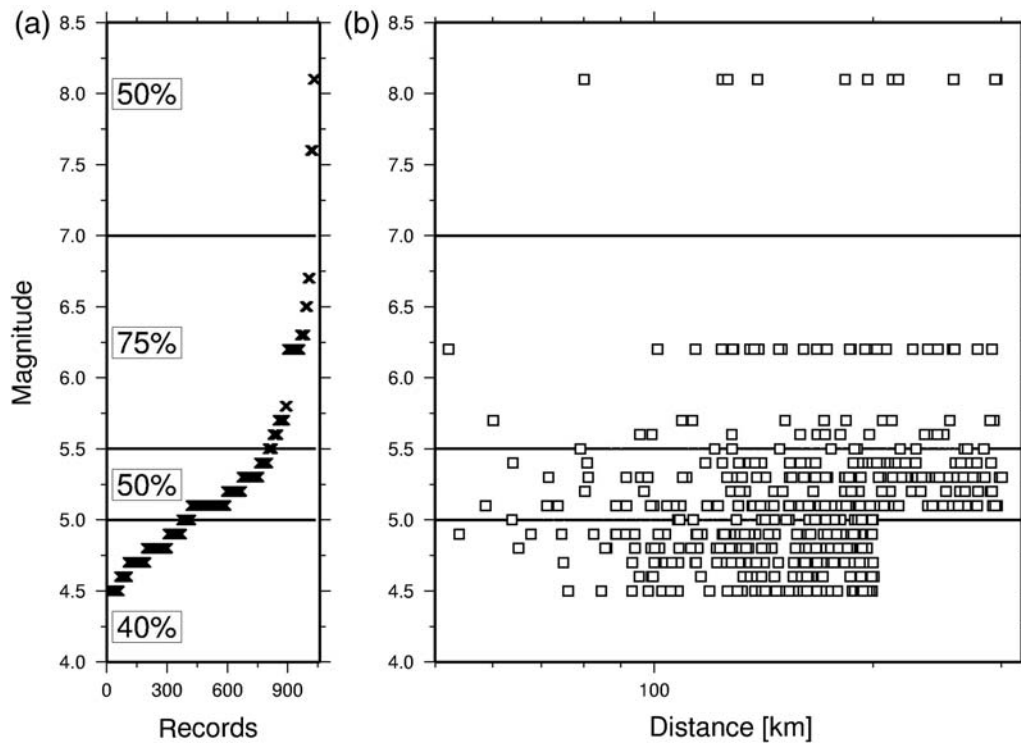
Figure 6. (a) Distribution of the magnitude for the considered data set. The percentages correspond to the fraction of earthquakes within each considered magnitude interval selected for calibrating the model. (b) Magnitude versus distance scatter plot for one of the 1000 created validation data sets.

40% of the events with $M_w < 5$ (corresponding to 20 events over 50), 50% of the events with magnitude between 5 and 5.5 (18 events over 36), and 75% of the events in the range 5.5–7 (13 events over 18) are selected (Fig. 6a). One of the two largest events (either 8.1 or 7.6) is included, whereas the other is used for the validation. The percentage of data included in the calibration data sets for different magnitudes is arbitrarily chosen, with the aim of creating a set of balanced calibration data sets with enough data to constrain the testing models. Tests performed by varying the boundaries of the magnitude intervals and the percentages used to populate them show that, for reasonable choices for these parameters, similar results are obtained, without significant changes in the main conclusions of the validation tests. The random selection is repeated 1000 times, leading to 1000 models that can be tested against independent data. One example of the validation data set is shown in Figure 6b.

The results of the validation are shown in Figure 7. The comparison shown in the top panels with the bootstrap results obtained from the original data set confirms the attenuation models and station corrections obtained with the 1000 randomly selected calibration data sets are reliable. The distribution of the magnitude difference shows a small bias equal to −0.049 with sigma 0.22. When the mainshock is included, the magnitude of the largest aftershock is well predicted, and the same occurs for the M_w 8.1 mainshock when

the M_w 7.6 aftershock is included. It is worth noting that in the latter case the magnitude of the mainshock is well predicted despite the fact that in this case an extrapolation of the model toward higher magnitude is necessary.

Application and Conclusions

The attenuation function derived in this note can be applied to compute magnitude values equivalent to M_w for the whole seismic sequence. In particular, exploiting the IPOC strong-motion network, an equivalent M_w can be computed for those cases when the automatic moment tensor analysis is hampered by overlapping phase arrivals at regional/teleseismic distances, or for local earthquakes with reduced signal-to-noise ratio at regional distances. The possibility of extrapolating the model down to magnitude 4 is still under evaluation. As an example, the calibrated magnitude scale is applied to an early aftershock, which occurred about 155 s after the mainshock. At regional/teleseismic distances, its phase arrivals are overwhelmed by coda of the mainshock (see examples in Fig. 8). This makes the determination of the source parameter difficult, in particular, in an automatic processing scheme. In contrast, the waveform of the early aftershock is clearly visible in the local strong-motion data. The station magnitudes computed for the early aftershock are shown in Figure 9, considering nine IPOC stations within 300 km from the hypocenter, for which reliable estimates
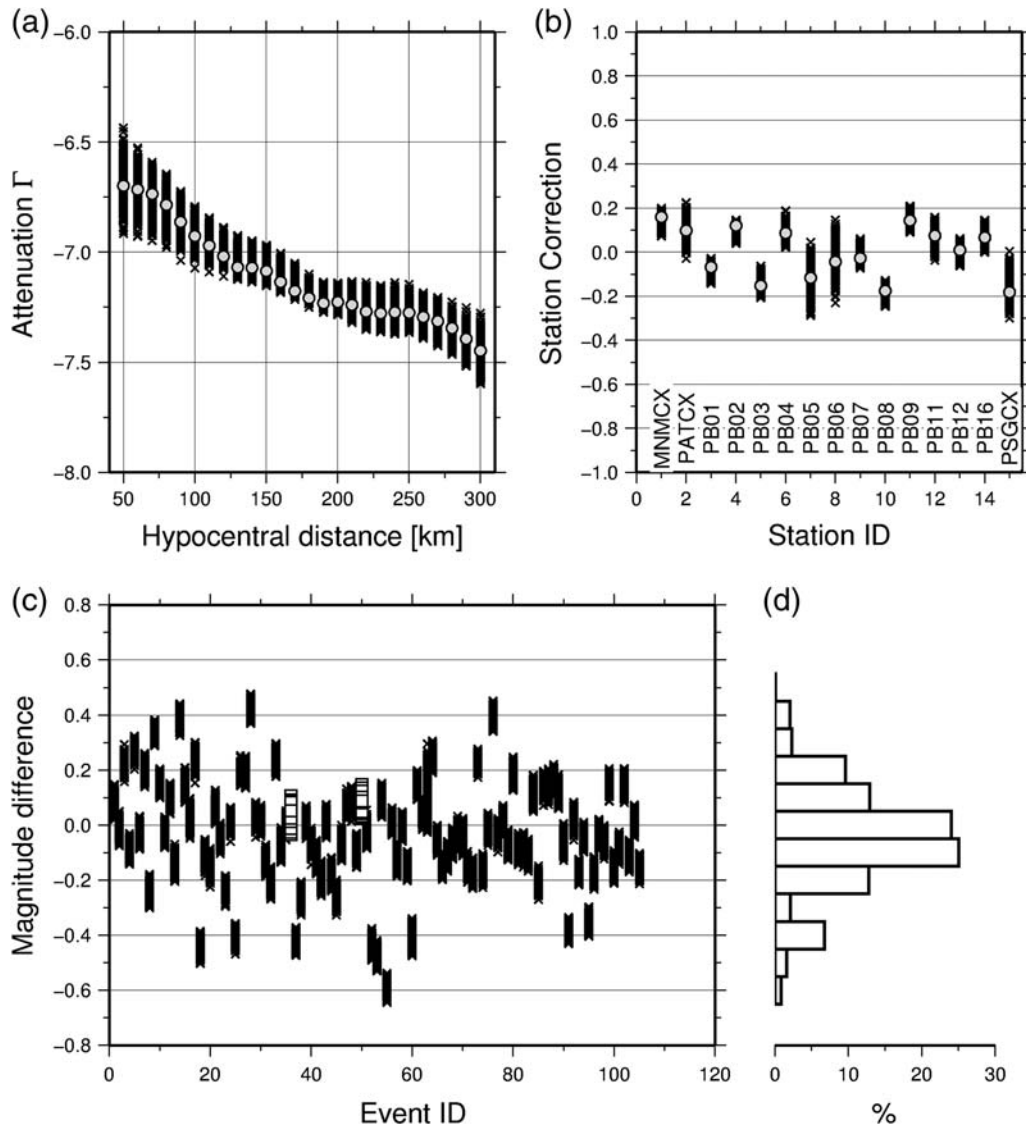
Figure 7. Results of the validation analysis. In the top, the 1000 calibrated models (crosses) are compared with the mean bootstrap solutions (circles), for (a) attenuation and (b) station corrections. (c) The differences between the magnitude computed for each validation earthquake and the M_w from bulletin are shown (each single cross represents the value computed considering one of the 1000 calibrated model). The results for the M_w 8.1 mainshock and the M_w 7.6 aftershock are shown as empty squares. (d) The histogram of the differences is shown.

of PGD are obtained. We obtained an average magnitude of 6.6, with a standard deviation of 0.3. Hence, the early aftershock is currently the second largest aftershock. It occurred south of the mainshock and toward the location of the M_w 7.6 aftershock, which struck two days later (see stars in Fig. 1). The application of the derived magnitude scale to the whole seismic sequence is foreseen as a worthwhile exercise, to create a strong-motion data set with homogeneous magnitude, suitable for studies on ground-motion prediction equations.

Data and Resources

The strong-motion data used in the present study have been collected within the Integrated Plate boundary Observatory Chile (http://www.ipoc-network.org) initiative.

The data analyzed in this study have been downloaded from GEOFON repository at http://geofon.gfz-potsdam.de/. Although the bulletin information is freely available (http://geofon.gfz-potsdam.de/eqinfo/eqinfo.php), the strong-motion data are restricted to allowed users at the time of writing this note (http://geofon.gfz-potsdam.de/waveform/archive/network.php?ncode=CX). Information about the IPOC network is available through the project webpage (http://www.ipoc-network.org/index.php/observatory.html). ASCN data shown in Figure 7 have been downloaded from Incorporated Research Institutions for Seismology Data Management Center using fdsnws-dataselect. Figures have been drawn using the Generic Mapping Tool software (http://gmt.soest.hawaii.edu/). All of the above websites were last accessed on May 2014.

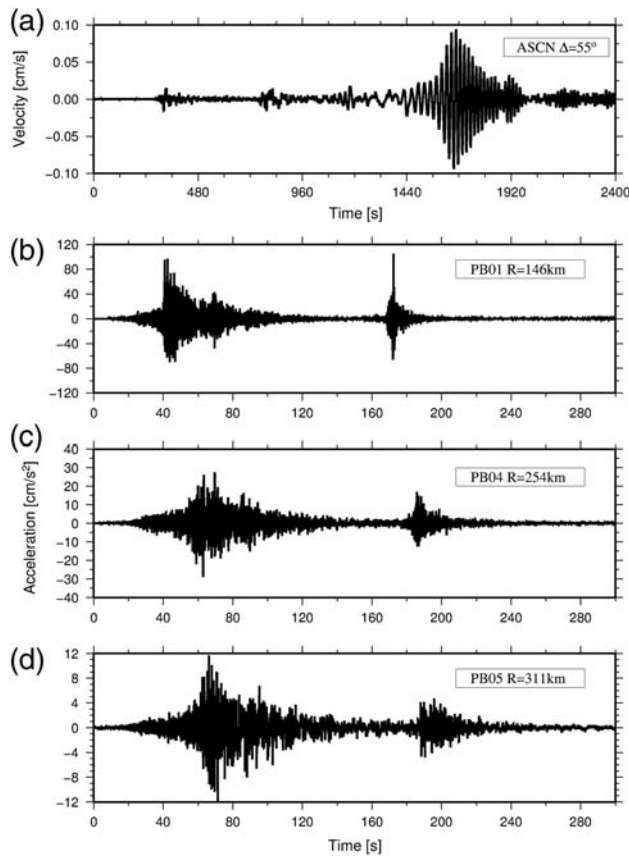**Figure 8.** (a) Broadband registration (vertical component) at station ASCN (mainshock epicentral distance Δ = 55°) including the mainshock and the early aftershock. (b)–(d) Examples of strong-motion waveforms (east–west component) of the mainshock and early aftershock as recorded at some IPOC strong-motion stations (the station name and the hypocentral distance of the early aftershock are indicated inside each frame).
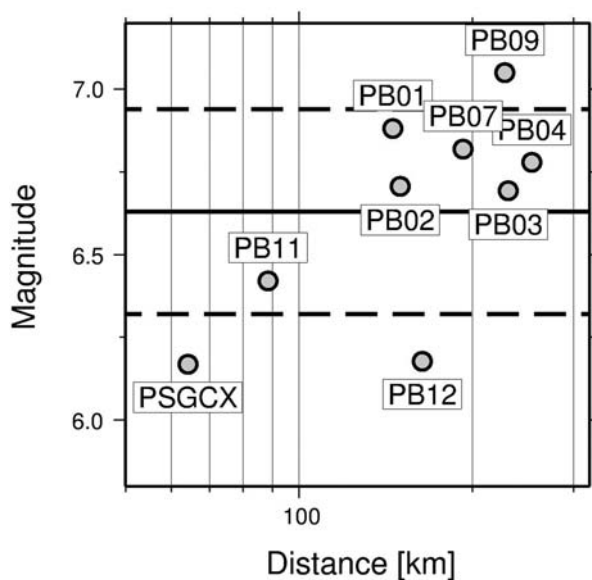

Figure 9. Station magnitudes for the early aftershock. The average (black line) ±1 standard deviation (broken lines) are also shown.

References

Al Atik, L., N. A. Abrahamson, J. J. Bommer, F. Scherbaum, F. Cotton, and N. Kuehn (2010). The variability of ground-motion prediction models and its components, *Seismol. Res. Lett.* **81,** no. 5, 794–801, doi: 10.1785/gssrl.81.5.794.

Bindi, D., S. Parolai, E. Görgün, H. Grosser, C. Milkereit, M. Bohnhoff, and E. Durukal (2007). ML scale in northwestern Turkey from 1999 Izmit aftershocks: Updates, *Bull. Seismol. Soc. Am.* **97,** 331–338.

Castro, R. R., J. G. Anderson, and S. K. Singh (1990). Site response, attenuation and source spectra of S waves along the Guerrero, Mexico, subduction zone, *Bull. Seismol. Soc. Am.* **80,** 1481–1503.

DeMets, C., R. G. Gordon, and D. F. Argus (2010). Geologically current plate motions, *Geophys. J. Int.* **181,** 1–80, doi: 10.1111/j.1365-246X.2009.04491.x.

Efron, B. (1979). Bootstrap methods, another look at the jacknife, *Ann. Stat.* **7,** 1–26.

Kelleher, J. A. (1972). Rupture zones of large South American earthquakes and some predictions, *J. Geophys. Res.* **77,** no. 11, 2087–2103.

Paolucci, R., F. Pacor, R. Puglia, G. Ameri, C. Cauzzi, and M. Massa (2011). Record processing in ITACA, the new Italian strong-motion database, in *Earthquake Data in Engineering Seismology. Predictive Models, Data Management and Networks. Geotechnical, Geological and Earthquake Engineering Series*, Chapter 8, S. Akkar, P. Gulkan, and T. Van Eck (Editors), Vol. 14, Springer, Dordrecht, The Netherlands, 99–113.

Savage, M. K., and J. G. Anderson (1995). A local-magnitude scale for the western Great basin–eastern Sierra Nevada from synthetic Wood–Anderson seismogram, *Bull. Seismol. Soc. Am.* **85,** 1236–1243.

Schurr, B., G. Asch, S. Hainzl, J. Bedford, A. Hoechner, M. Palo, R. Wang, M. Moreno, M. Bartsch, Y. Zhang, O. Oncken, F. Tilmann, T. Dahm, P. Victor, S. Barrientos, and J.-P. Vilotte (2014). Gradual unlocking of plate boundary controlled initiation of the 2014 Iquique earthquake, *Nature* **512,** 299–302, doi: 10.1038/nature13681.

Spallarossa, D., D. Bindi, P. Augliera, and M. Cattaneo (2002). An M_l scale in northwestern Italy, *Bull. Seismol. Soc. Am.* **92,** 2205–2216.

GFZ German Research Centre for Geosciences
Telegrafenberg, 14473 Potsdam, Germany
bindi@gfz-potsdam.de
    (D.B., B.S., A.S., S.P.)

INGV Sezione di Milano-Pavia
via Bassini 15
20133 Milano, Italy
    (R.P.)

INGV Sezione di Roma
Via di Vigna Murata 605
00143 Rome, Italy
    (E.R.)

ISTerre
LGIT, BP 53
38041 Grenoble Cedex 9, France
    (F.C.)